Seismic slip on an upper plate normal fault during a large subduction megathrust rupture

Stephen P. Hicks* and Andreas Rietbrock

Liverpool Earth Observatory, University of Liverpool

Address: Jane Herdman Laboratories, 4 Brownlow Street, Liverpool, L69 3GP

Email: s.hicks@liverpool.ac.uk

7 **Summary**

8 Quantification of stress accumulation and release during subduction zone seismic cycles

9 requires an understanding of the distribution of fault slip during earthquakes. Reconstructions

10 of slip are typically constrained to a single, known fault plane. Yet, slip has been shown to

11 occur on multiple faults within the subducting plate[1] due to stress triggering[2], resulting in

12 phenomena such as earthquake doublets[3]. However, rapid stress triggering from the plate

13 interface to faults in the overriding plate has not been documented. Here we analyse seismic

14 data from the magnitude 7.1 Araucania earthquake that occurred in the Chilean subduction zone

15 in 2011. We find that the earthquake, which was reported as a single event in global moment

16 tensor solutions[4,5], was instead composed of two ruptures on two separate faults. Within 12

17 seconds, a thrust earthquake on the plate interface triggered a second large rupture on a normal

18 fault 30 km away, in the overriding plate. This configuration of partitioned

19 rupture is consistent with normal-faulting mechanisms in the ensuing aftershock sequence. We

20 conclude that plate interface rupture can trigger almost instantaneous slip in the overriding plate

21 of a subduction zone. This shallow upper plate rupture may be masked from teleseismic data,

22 posing a challenge for real-time tsunami warning systems.

Main body

A recent succession of large ($M_w > 8$) earthquakes in circum-Pacific subduction zones has focussed attention on the relationship between physical properties and stress distribution along the megathrust plate interface. Seismic ruptures along the megathrust can be viewed as smooth and spatially varying patches of slip on a single fault; in this case, the subducting plate interface[6]. The fault geometry used in early coseismic slip models is underpinned by centroid moment tensor (CMT) solutions often reported by earthquake monitoring agencies. Although more sophisticated slip inversions use curved faults based on regional subduction geometry[7], slip is nearly always assigned to a single fault.

An alternative rupture configuration is slip occurring on separate faults due to static or dynamic triggering processes[2], resulting in phenomena such as doublets[3]. A doublet is the occurrence of two nearby earthquakes with similar magnitude. The time delay between ruptures can range from months[3] to seconds[1]. Many documented cases of subduction zone doublets involve triggering between the subducting plate interface and deep-rooted faults in the downgoing plate[3,8]. Although the implications for tsunami hazard are significant, there are no reported cases of rapid triggering from the plate interface to the upper plate, where there are complex faulting networks[9,10]. To resolve triggered faulting in such cases, dense local seismic observations are needed.

A region with a suitably dense network of seismometers is the central Chile subduction zone following the M_w 8.8 Maule earthquake in 2010. The ensuing aftershock sequence was captured in detail by the International Maule Aftershock Deployment[11]. Here, we focus on the largest interplate aftershock of the Maule sequence: the M_w 7.1 Araucania earthquake that occurred on 2 January 2011 at 20:20:18 UTC. Based on CMT solutions derived from teleseismic waveforms, the Araucania earthquake appears to be a 'straightforward' plate interface thrusting

3

47   event[4,5]. Its epicentre (Supplementary Note 1, Supplementary Table 1) lies in a region that acted

48   as a barrier during the 1960 M_w 9.5 Valdivia[12] and 2010 M_w 8.8. Maule[6,11] earthquakes (Fig. 1).

49   Moreover, the upper plate in this region is heavily faulted[6,10]. Therefore, the Araucania

50   earthquake is an ideal candidate to examine possible interactions between the plate interface

51   and upper plate faults.

52   We employed a multiple point-source inversion of regional seismic data[13,14]. Compared to

53   conventional slip inversions along pre-defined fault planes[6] and single point-source CMT

54   inversions[5], we can retrieve centroid times of sub-events and permit multiple faulting styles on

55   a grid of trial point-sources. A detailed understanding of 3-D crustal velocity structure[15,16]

56   ensures robust waveform inversion. Synthetic tests (Supplementary Note 2) show that we can

57   accurately resolve a range of extended source configurations involving offshore rupture using

58   the available station distribution.

59   Using the observed data, we first investigated whether low-frequency waveforms (0.02–0.04

60   Hz) in the near-field could represent the earthquake as a single point-source. The optimal

61   regional CMT solution provides a good fit to the observed waveforms at most stations

62   (Supplementary Figure 2). The centroid lies close to our relocated epicentre; its mechanism is

63   consistent with the teleseismic GCMT and USGS solutions (Fig. 1), indicating thrusting along

64   the plate interface. A high double-couple percentage (%DC) indicated by the global (98%) and

65   our regional solutions (85%) suggests a simple faulting mechanism. When we increase the

66   upper frequency limit to >0.06 Hz, waveform variance reduction (VR) sharply decreases and,

67   at the upper limit of 0.08 Hz, we notice two clear arrivals in the observed waveforms (Fig. 1b

68   & Supplementary Figure 3). Therefore, the next step is to consider whether a complex source

69   can be resolved using higher frequency waveforms and a multiple point-source

70   parameterisation.

4

71   A two-point-source model is a logical progression; an $M_w \sim 7$ earthquake likely comprises no

72   more than two to three patches of slip[17]. Compared with that of using the first source alone (VR

73   = 0.57), introduction of the second source significantly increases the waveform fit (Fig. 2a) by

74   30% (VR = 0.73), which is statistically significant to within the 99.5% confidence interval

75   (Supplementary Note 3). Mechanisms at each trial point-source position are very consistent,

76   with sharp correlation maxima (Fig. 2b). Based on our results, we can confidently identify the

77   following sequence of events, which can be regarded as a closely-spaced doublet (CSD), both

78   in time and space. Following nucleation, Event I (M_w 6.8) ruptured the megathrust beneath the

79   coast. No more than twelve seconds later, Event II (M_w 6.7) ruptured to the southwest at a

80   shallower depth and with an oblique normal faulting mechanism (Fig. 2).

81   Locations and mechanisms of aftershocks (Supplementary Note 4) that followed the Araucania

82   earthquake support this CSD configuration. From our 44 relocated events, it is clear that there

83   are two distinct groups of aftershocks (Fig. 3a). One group is located in the coastal region

84   (hereafter, Group A); the other 30–40 km to the southwest (hereafter, Group B). Group B

85   aftershocks have shallower depths, located within the marine forearc, up to 9 km above the

86   plate interface (Fig. 3b). We obtained 19 robust CMT solutions from this aftershock sequence

87   (Fig. 3), all of which have depths in agreement with their hypocentral location, based on a 3-D

88   velocity model and ocean-bottom observations[15]. Normal faulting mechanisms dominate

89   aftershock Group B. Group A aftershocks comprise mixed mechanisms, but interplate thrust

90   faulting is most common.

91   A puzzling location discrepancy between Event II and aftershock Group B (Supplementary

92   Figure 4) leads us to assess location bias in the multiple point-source inversion. So far, we have

93   computed synthetic seismograms by calculating Green's functions in a 1-D velocity model.

94   However, in the shallow regions of subduction zones, there are strong lateral velocity gradients

95   (Figs. 3 & Supplementary Figure 5), particularly in S-wave velocity. Therefore, a more realistic

96   velocity model can improve waveform fits and make source inversions more stable. To account

97   for lateral velocity variations, we simulated waveforms in a 3-D velocity model[15,16] using the

98   spectral element code SPECFEM3D[18]. We used 3-D synthetics based on our two-point-source

99   solution as input to a multiple point-source inversion using 1-D Green's functions. While the

100   position of Event I remains stable, we find that the inversion shifts Event II 12 km to the south

101   (from position 16 to 15; Supplementary Figure 6). Similarly, when we simulate the waveforms

102   from Event II at the location of aftershock Group B (position 17), we find a similar southward

103   shift, as implied from the real data inversion. Therefore, it is likely that Event II occurred ~12

104   km northward with respect to the formal inversion result of Fig. 2b (Supplementary Table 5).

105   This result demonstrates the importance of 3-D structural models to obtain accurate source

106   parameters of offshore subduction earthquakes.

107   Based on our aftershock analyses and 3-D waveform simulations it is now clear that Event II

108   ruptured on a normal fault near the base of the overriding crust (Figs. 3 & 4). Group B

109   aftershocks are located close to the prominent Mocha-Villarrica fault zone (Fig. 3). This fault

110   may be related to strong velocity contrasts in the marine forearc beneath Isla Mocha, where

111   Group B aftershocks are located (Figs. 3 & 4). Crustal faulting in the region is pervasive and

112   may extend through the entire crust[10,19]; it is plausible that the geometry of fault networks

113   becomes more complex at the base of the forearc with possible conjugate faulting (Fig. 4). We

114   speculate that these faults are compressional during the interseismic period, but a stress

115   inversion following the Maule earthquake[20] may favour post-seismic extension. Based on

116   approximate fault areas from scaling relations[21], the two fault planes of Events I and II likely

117   do not intersect. There are several possible mechanisms for the triggering of a rupture by a

118   preceding earthquake. Dynamically triggered rupture of the normal fault is likely the dominant

119   failure mechanism given that Event II's centroid time coincides with the passage of high-

120   amplitude S-wave arrivals from Event I (Supplementary Figure 7). However, we cannot

121   completely rule out static stress transfer acting as a partial trigger.

122   To our knowledge, these results provide the first documented case of plate interface thrusting

123   instantaneously activating a large rupture in the overriding plate through dynamic triggering.

124   Past subduction zone doublets have been identified by high non-double components in their

125   CMT solutions[8]. Conversely, in the case of the Araucania earthquake, the low-frequency single

126   point-source solutions of both the global and regional CMT solutions did not yield a low %DC

127   (Fig. 1). This discrepancy is also evidenced by our synthetic tests. It is possible that the short

128   time delay and small distance between Events I and II masks rupture complexity in teleseismic

129   CMT solutions. Therefore, CSDs may be completely hidden from global networks. CSDs may,

130   however, be detected from a greater proportion of high frequency radiation in regional

131   waveforms (Supplementary Note 5, Supplementary Figure 8), although this character may

132   depend on several other source parameters, such as rupture duration. CMT solutions provided

133   by global reporting agencies are accepted by the seismological community and form the basis

134   of slip inversions and examinations of the stress field. CMTs are, therefore, a pillar of

135   earthquake science, yet our results recommend their careful use in the case of slip on multiple

136   fault planes.

137   The precedent set by this study also presents a new perspective for tsunami hazard assessment

138   in subduction zones. Reverse faults as well as normal faults could theoretically be immediately

139   triggered by megathrust slip, causing large seafloor displacement. A wide variety of upper plate

140   faults are present in many subduction zones. For example, steeply-dipping normal faults have

141   been imaged in the upper plate along the N. Chile and S. Peru margins[9]. Furthermore, a large

142   upper-plate reverse faulting event preceded the 2014 M_w 8.2 Pisagua, N. Chile earthquake[22] and

143   backthrust faults are widespread in the Sumatra subduction zone[23]. An M_w 7.0 rupture in the

144   upper plate could result in substantial vertical seafloor displacement of 1.2 m (Supplementary

7

145   Note 6). If this scenario were scaled up to a larger rupture (M_w ~7.5), slip on the forearc fault

146   could cause a localised tsunami on the continental shelf, although the upper limit of rupture size

147   is controlled by the geometry and frictional properties of these faults (Fig. 3). A tsunami may

148   be caused by static vertical displacement or through submarine landslides (Fig. 4), which have

149   occurred locally in the past[24]. Yet without local strong-motion instruments, GPS networks, or

150   close inspection of regional waveforms, near-field triggered ruptures will be difficult to detect.

151   We speculate that the lack of evidence for Event II in single-source CMT solutions may result

152   in part from the short timing between the two sources. Therefore, we recommend that the

153   capability of teleseismic CMT inversions to resolve different doublet configurations is given a

154   full assessment. Furthermore, there is a need to re-evaluate CMT solutions for large earthquakes

155   using local and regional waveforms in subduction zones globally to examine whether CSDs

156   involving the upper plate are ubiquitous.

157

References

1. Lay, T., Duputel, Z., Ye, L. & Kanamori, H. The December 7, 2012 Japan Trench intraplate doublet (Mw 7.2, 7.1) and interactions between near-trench intraplate thrust and normal faulting. *Phys. Earth. Planet. Inter.* **220,** 73–78 (2013).

2. Freed, A. M. Earthquake triggering by static, dynamic, and postseismic stress transfer. *Annu. Rev. Earth Planet. Sci.* **33,** 335–367 (2004).

3. Ammon, C. J., Kanamori, H. & Lay, T. A great earthquake doublet and seismic stress transfer cycle in the central Kuril islands. *Nature* **451,** 561–565 (2008).

4. United States Geological Survey National Earthquake Information Center. M7.2 - Araucania, Chile. (2011). at <http://earthquake.usgs.gov/earthquakes/eventpage/usp000hsfq#scientific_tensor>

5. Ekström, G., Nettles, M. & Dziewoński, A. M. The global CMT project 2004–2010: Centroid-moment tensors for 13,017 earthquakes. *Phys. Earth. Planet. Inter.* **200-201,** 1–9 (2012).

6. Moreno, M. *et al.* Toward understanding tectonic control on the Mw 8.8 2010 Maule Chile earthquake. *Earth Planet. Sci. Lett.* **321–322,** 152–165 (2012).

7. Hayes, G. P., Wald, D. J. & Johnson, R. L. Slab1. 0: A three- dimensional model of global subduction zone geometries. *J. Geophys. Res.* **117, B1** (2012).

8. Lay, T. *et al.* The 2009 Samoa-Tonga great earthquake triggered doublet. *Nature* **466,** 964–968 (2010).

9. Audin, L., Lacan, P., Tavera, H. & Bondoux, F. Upper plate deformation and seismic barrier in front of Nazca subduction zone: The Chololo Fault System and active tectonics along the Coastal Cordillera, southern Peru. *Tectonophysics* **459,** 174–185 (2008).

10. Melnick, D., Bookhagen, B., Strecker, M. R. & Echtler, H. P. Segmentation of megathrust rupture zones from fore-arc deformation patterns over hundreds to millions of years, Arauco peninsula, Chile. *J. Geophys. Res. Solid Earth* **114,** B01407 (2009).

11. Rietbrock, A. *et al.* Aftershock seismicity of the 2010 Maule Mw= 8.8, Chile, earthquake: Correlation between co-seismic slip models and aftershock distribution? *Geophys. Res. Lett.* **39,** L08310 (2012).

12. Moreno, M. S., Bolte, J., Klotz, J. & Melnick, D. Impact of megathrust geometry on inversion of coseismic slip from geodetic data: Application to the 1960 Chile earthquake. *Geophys. Res. Lett.* **36,** L16310 (2009).

13. Sokos, E. & Zahradnik, J. A Matlab GUI for use with ISOLA Fortran codes. *Users' guide* (2006).

14. Zahradnik, J., Serpetsidaki, A., Sokos, E. & Tselentis, G.-A. Iterative Deconvolution of Regional Waveforms and a Double-Event Interpretation of the 2003 Lefkada Earthquake, Greece. *B. Seismol. Soc. Am.* **95,** 159–172 (2005).

15. Hicks, S. P., Rietbrock, A., Ryder, I. M. A., Lee, C.-S. & Miller, M. Anatomy of a megathrust: The 2010 M8.8 Maule, Chile earthquake rupture zone imaged using seismic tomography. *Earth Planet. Sci. Lett.* **405,** 142–155 (2014).

16. Haberland, C., Rietbrock, A., Lange, D., Bataille, K. & Dahm, T. Structure of the seismogenic zone of the southcentral Chilean margin revealed by local earthquake

200   traveltime tomography. *J. Geophys. Res.* **114,** B01317 (2009).

201 17. Zahradnik, J. & Sokos, E. The Mw 7.1 Van, Eastern Turkey, earthquake 2011: two-point
202   source modelling by iterative deconvolution and non-negative least squares. *Geophys. J.*
203   *Int.* **196,** 522–538 (2014).

204 18. Komatitsch, D., Erlebacher, G., Göddeke, D. & Michéa, D. High-order finite-element
205   seismic wave propagation modeling with MPI on a large GPU cluster. *J. Comput. Phys.*
206   **229,** 7692–7714 (2010).

207 19. Hicks, S. P., Nippress, S. E. & Rietbrock, A. Sub-slab mantle anisotropy beneath south-
208   central Chile. *Earth Planet. Sci. Lett.* **357,** 203–213 (2012).

209 20. Hardebeck, J. L. Coseismic and postseismic stress rotations due to great subduction zone
210   earthquakes. *Geophys. Res. Lett.* **39,** L21313 (2012).

211 21. Blaser, L., Krüger, F., Ohrnberger, M. & Scherbaum, F. Scaling Relations of Earthquake
212   Source Parameter Estimates with Special Focus on Subduction Environment. *B. Seismol.*
213   *Soc. Am.* **100,** 2914–2926 (2010).

214 22. González, G. *et al.* Upper plate reverse fault reactivation and the unclamping of the
215   megathrust during the 2014 northern Chile earthquake sequence. *Geology* G36703.1
216   (2015).

217 23. Singh, S. C. *et al.* Evidence of active backthrusting at the NE Margin of Mentawai Islands,
218   SW Sumatra. *Geophys. J. Int.* **180,** 703–714 (2010).

219 24. Geersen, J., Völker, D., Behrmann, J. H., Reichert, C. & Krastel, S. Pleistocene giant slope
220   failures offshore Arauco Peninsula, Southern Chile. *J. Geol. Soc. London* **168,** 1237–1248
221   (2011).

222 25. Quintero, R., Zahradnik, J. & Sokos, E. Near-regional CMT and multiple-point source
223   solution of the September 5, 2012, Nicoya, Costa Rica Mw 7.6 (GCMT) earthquake. *J. S.*
224   *Am. Earth Sci.* **55,** 155–165 (2014).

225 26. Sokos, E. & Zahradnik, J. Evaluating Centroid- Moment- Tensor Uncertainty in the New
226   Version of ISOLA Software. *Seismol. Res. Lett.* **84,** 656–665 (2013).

227 27. Casarotti, E. *et al.* in *Proceedings of the 16th International Meshing Roundtable* 579–597
228   (Springer Berlin Heidelberg, 2008).

229 28. Frohlich, C. Triangle diagrams: ternary graphs to display similarity and diversity of
230   earthquake focal mechanisms. *Phys. Earth. Planet. Inter.* **75,** 193–198 (1992).

231 29. Hayes, G. P. *et al.* Seismotectonic framework of the 2010 February 27 Mw 8.8 Maule,
232   Chile earthquake sequence. *Geophys. J. Int.* **195,** 1034–1051 (2013).

233 30. Melnick, D. & Echtler, H. P. in *The Andes* 565–568 (Springer Berlin Heidelberg, 2006).
234   doi:10.1007/978-3-540-48684-8_30

235

Supplementary information

Supplementary information is linked to the online version of the paper at www.nature.com/nature.

Acknowledgments

Author contributions

S.P.H. carried out the single and multiple point-source inversions, as well as the moment tensor inversion and aftershock relocations. S.P.H. wrote the manuscript, interpreted the results, and generated all figures. A.R. carried out the 3-D full waveform simulations, wrote the manuscript, and interpreted the results.

Author information

Reprints and permissions information is available at www.nature.com/reprints.

The authors declare no competing financial interests.

Correspondence and requests for materials should be addressed to S.P.H (s.hicks@liverpool.ac.uk) or A.R. (a.rietbrock@liverpool.ac.uk).

255 **Figure Captions**

Fig. 1: Location and single source solution. a) Location map. Stations used for CMT inversion are labelled with station codes. Other stations are for hypocentre relocation only (Supplementary Note 1). Shading indicates rupture areas of great earthquakes in 1960[12] and 2010[6]. Inset: Regional tectonic setting. b) Double-couple percentage (%DC) and variance reduction (VR) of the single point-source versus frequency. A transition occurs at 0.057 Hz, where VR suddenly decreases because the waveforms cannot be explained by a single source alone. This change is illustrated by representative waveforms at low and high frequencies (see Supplementary Figure 2 & Supplementary Figure 3 for details).

256

Fig. 2: Two-point-source solution. a) Observed (black) and synthetic (red) waveforms for the optimum high-frequency (0.02–0.08 Hz) solution. Station names are labelled. Numbers alongside each waveform component denote VR. Blue and green shading denotes the contribution from each event. b) Waveform correlation for each event as a function of trial point-source position (numbered). The optimum time shift of Event I and II is shown. Black beach balls are solutions that lie within 90% of the optimum solution's (red beach ball) VR. The red star denotes the earthquake's epicentre. c) Resulting moment-rate function obtained using the NNLS method.

257

Fig. 3: Aftershock analysis. (a) Map and (b) cross-section showing locations and focal mechanisms of aftershocks (Groups A and B) and mainshock events (labelled EV-I and EV-II). Faulting style is classified on principal stress orientations[28] and minimum rotation angle with respect to plate interface thrust faulting[29], accounting for plate interface geometry (black line)[15,16]. We plot the revised location of Event II, based on 3-D waveform modelling. Mapped faults are shown[10,30]; MVFZ = Mocha-Villarrica fault zone. The cross-section background is from P-wave velocity tomography models[15,16]. The star denotes the hypocentre of the Araucania earthquake; the triangle shows the coastline.

258

Fig. 4: Schematic interpretation of the Araucania earthquake rupture. Plate interface thrusting (Event I) triggered a rupture along an extensional fault in the overriding plate (Event II). It is likely that two great earthquakes in 1960 and 2010 brought both faults closer to failure. As shown by ancient submarine landslide deposits in the area, a larger-scale rupture in the overriding plate has the potential to act as a tsunamigenic earthquake. Beach balls represent the focal mechanisms of both events from Fig. 3. The inset shows the interpreted structure of conjugate normal faulting with the background colour representing v_p/v_s ratio[15].
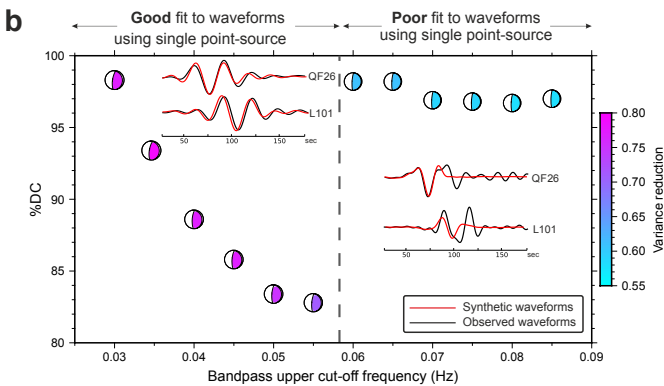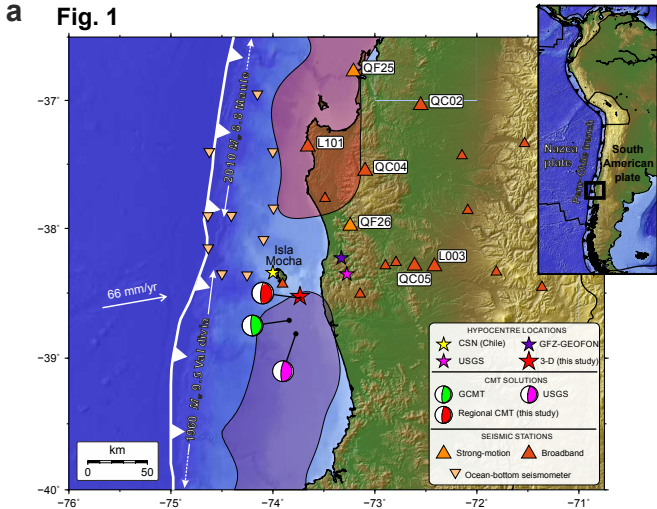
Fig. 1

a

QF25
QC02
L101
QC04
QF26
QC05
L003

Isla
Mocha

66 mm/yr

km
0   50

Nazca
plate

South
American
plate

HYPOCENTRE LOCATIONS
★ CSN (Chile)   ★ GFZ-GEOFON
★ USGS   ★ 3-D (this study)

CMT SOLUTIONS
◓ GCMT   ◓ USGS
◓ Regional CMT (this study)

SEISMIC STATIONS
▽ Strong-motion   ▽ Broadband
▽ Ocean-bottom seismometer

b

← **Good** fit to waveforms   **Poor** fit to waveforms →
using single point-source   using single point-source

QF26
L101

QF26
L101

— Synthetic waveforms
— Observed waveforms

Fig. 2

Fig. 3

a

FAULT TRACES
Reverse   Transpressional
Blind fault

FAULTING MECHANISMS
Interplate thrust   Normal
Intraplate reverse   Strike-slip

EV-I
EV-II
A
B
MVFZ
X   X'
40 km

b

Distance from trench (km)
0   25   50   75   100   125

X   X'

Frontal accretionary prism   Isla   Paleo-accretionary   Continental
                             Mocha   wedge   Forearc Crust

Subducting plate interface

Depth (km)

EV-II
EV-I

v_p (km/s)
4.0 4.5 5.0 5.5 6.0 6.5 7.0 7.5 8.0
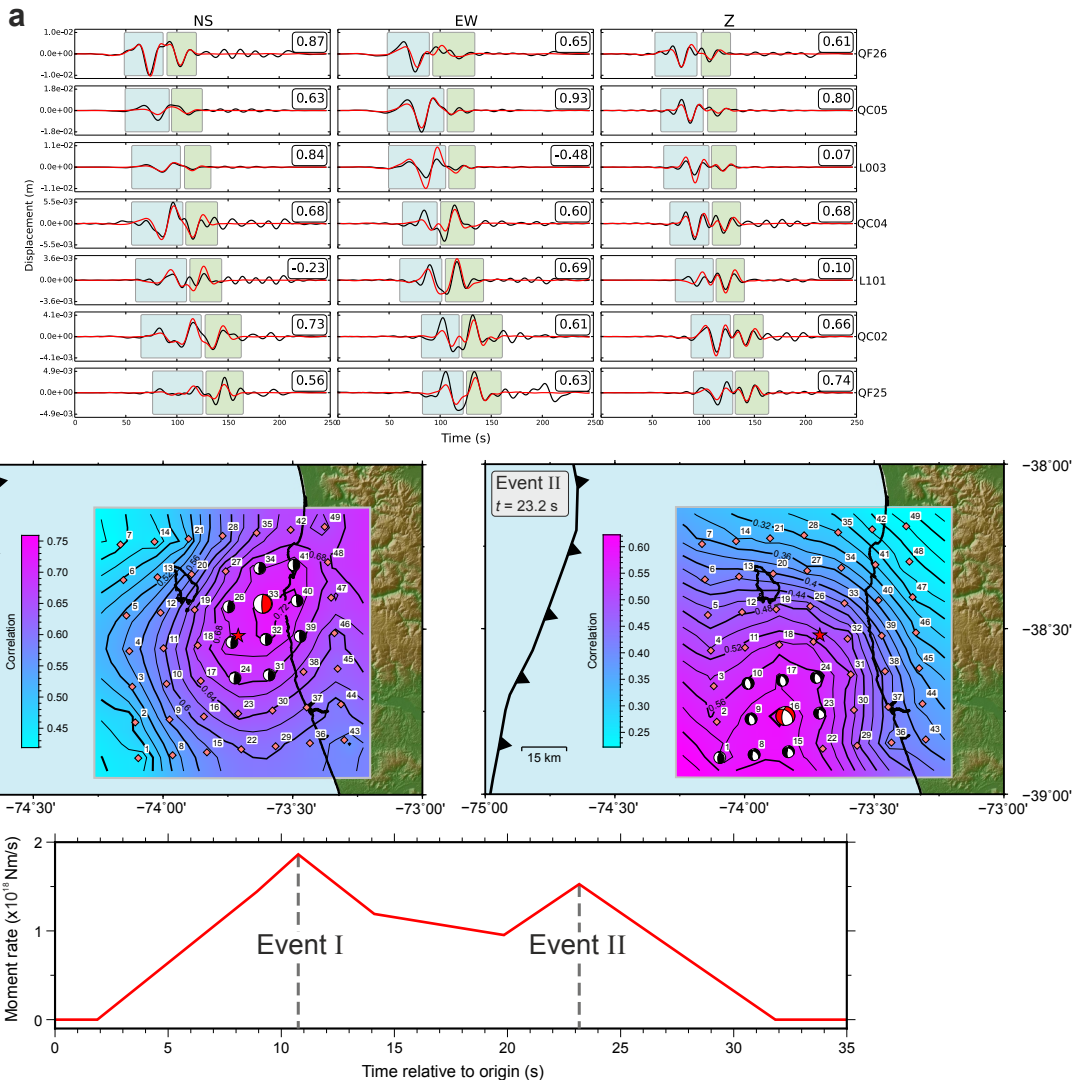
Fig 4. Vertical exaggeration: 2.5x. Horizontal scale: 40 km
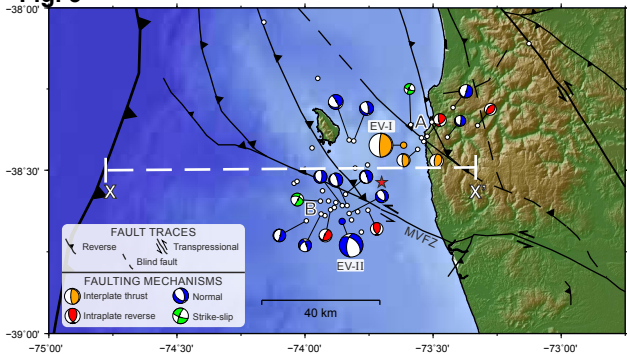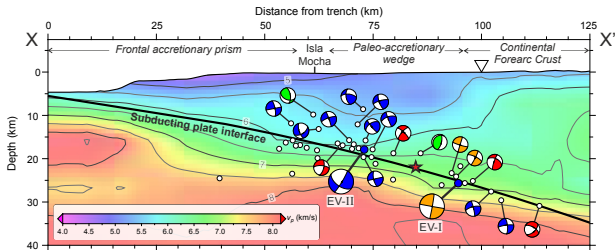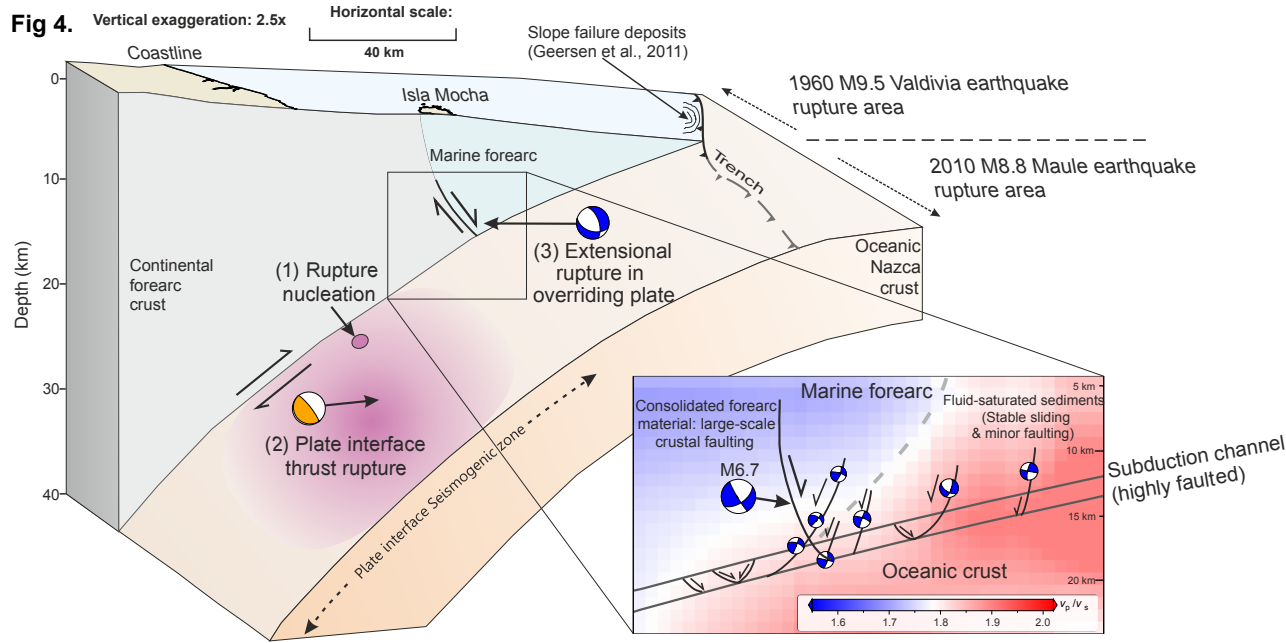
Methods

Data selection and processing

For the waveform inversion of the Araucania earthquake, we used broadband and strong-motion stations that were located onshore within an epicentral distance of 200 km from the Araucania earthquake. We only used waveforms from stations that have a high signal-to-noise ratio (> 10) in the frequency range 0.01–0.10 Hz (Supplementary Figure 9). Due to the close proximity of some stations to the earthquake, we excluded waveform records that were either clipped, had long period disturbances, or instrument tilt effects. These quality-control checks resulted in a set of seven stations (including two strong-motion stations) located north and east of the Araucania earthquake (Fig. 1a).

Source inversion algorithm

Iterative deconvolution (ID)[14] is used for the multiple point-source inversion of deviatoric moment tensors. ID works by inverting for the optimum focal mechanism and timing of sources for a prescribed set of points to minimise the L2 misfit between observed and synthetic waveforms. A grid search is then performed to select the source position that produces the highest correlation between observed and synthetic waveforms. The first inversion explains the full waveforms using a single source, the synthetics of which are then subtracted from the observed waveforms. The remaining waveforms are then used to invert for subsequent sub-events[14]. After the retrieval of each sub-event, VR is calculated and manually assessed to ensure that additional sub-events are required by the data and the waveforms are not just fitting correlated noise. For moment tensor inversion, we use the software package, ISOLA[13], which can be accessed athttp://seismo.geology.upatras.gr/isola/. In the inversion, the moment-rate of the source is prescribed; it is found by manually searching for the source length that produces the maximum VR. If the moment-rate of the source is shorter than the minimum inverted period,

16

285 then the source can be represented by a delta function. To negate artifacts produced by the ID

286 method, we also test the stability of our multiple point-source solution using a non-negative

287 least squares (hereafter, NNLS) inversion method[17]. In the NNLS approach, the double-couple

288 focal mechanism at each source is prescribed. At each trial point-source position, the moment

289 rate is represented by a set of shifted triangles. The weight of each triangle is then inverted for

290 using NNLS. In this paper, we use one-second triangle shifts. The moment of each source can

291 be constrained, which stabilises the inversion, although the exact value of total moment does

292 not dramatically influence source timings or positions[25].

293 The inversion is performed on bandpass-filtered displacement waveforms. The effect of

294 different 1-D velocity models was tested; the final solutions were calculated using a velocity

295 model appropriate for the coastline of south-central Chile (Supplementary Figure 10). We

296 analysed the effect of data errors and imperfect Green's functions by systematically removing

297 pieces of data from the inversion (jackknifing). Where subsurface structure is complex, removal

298 of certain stations may have a large effect on the final solution[26]. Based on the analysis of signal

299 to noise ratio (Supplementary Figure 9), we used a lowermost frequency limit of 0.02 Hz

300 throughout this paper. The upper frequency limit was dependent on the source parameterisation

301 used (single or multiple source).

302 **Single point-source inversion strategy**

303 Guided by preliminary inversions and the anticipated fault size[21], we used a trial point-source

304 grid with a spacing of 12 km in the down-dip and along-strike directions (Fig. 2b). At this stage,

305 we wanted to resolve the simplest possible source, so the maximum frequency was kept well

306 below the corner frequency (approximately 0.1 Hz for an $M_w \sim 7$ earthquake). Therefore, we

307 chose an upper frequency limit of 0.04 Hz and assumed a delta moment-rate function. We tested

308 the robustness of the solution by jackknifing stations and their individual components. The

17

309 source position changes slightly when varying the dataset, but by no more than 17 km

310 (Supplementary Figure 2); the largest shifts occur if the closest stations are removed from the

311 inversion. The zone of maximum correlation is not particularly sharp, corresponding to the

312 possible source locations from the jackknifing analysis (Supplementary Figure 2). These tests

313 show that the source location is reasonably stable and its mechanism is consistent throughout.

314 We also find that as the upper frequency bandpass cut-off increases, %DC gradually decreases.

315 This trend continues until around 0.057 Hz, above which, the full waveforms can only be

316 explained using Events I and II, and %DC becomes very high (Fig. 1b).

317 **Multiple point-source inversion strategy**

318 We first carried out a multiple point-source inversion using ID, in which the deviatoric moment

319 tensor mechanisms of both sources were allowed to vary. The grid of point-sources was kept

320 the same as for the single point-source inversion. For the source-time function, we found that

321 with increasing length of the triangle, the total moment gradually increases, while VR and %DC

322 of each source reaches a maximum at 18 s (Supplementary Figure 11). We therefore fixed the

323 triangle length of each source to 18 s for the ID multiple point-source inversion, although the

324 point-source mechanisms remain consistent for different triangle lengths, suggesting a stable

325 solution.

326 We used the NNLS method to test the robustness of the solution obtained by ID. To search for

327 the best-fitting source configurations, we performed two inversions: one in which total moment

328 was constrained by the ID solution; the other in which moment was allowed to vary. We tested

329 a number of source positions and faulting styles for Events I and II using the NNLS method,

330 but we found that the highest VR came from the two-point-source configuration found using

331 the ID method. Using the mechanisms given by the ID solution, we then performed a grid-

332 search over all possible combinations of the two-point-source locations using the NNLS

method. As expected, the moment-constrained inversion is most similar to the ID solution

(Supplementary Figure 12). Nevertheless, both inversions produce results consistent with the

ID solution. Importantly, the resulting source-time function obtained by NNLS shows that both

events have a similar time function to the 18 s triangle source used in ID (Fig. 2c). In summary,

we find no bias in the results caused by the inversion method.

As a further test of solution stability, we perform jackknifing tests by removing one station at

a time from the inversion. The results of these tests are shown in Supplementary Table 6 and

demonstrate remarkably consistent centroid positions and focal mechanisms for Events I and

II. The jackknifing test therefore indicates that the optimum multiple point-source solution is

not dependent on one single waveform. Furthermore, a three-point-source approximation did

not meaningfully improve the waveform fit (VR = 0.76; 3% increase in VR compared with

two-point-sources).

Since the ID method inverts for the first point-source before subsequently calculating the

second source, we carried out a test to determine whether Event II is dependent on the chosen

location and mechanism of Event I. Normally, we accept the source position that produces the

highest waveform correlation. However, for this test, we fixed the position of Event I and chose

the corresponding best-fitting mechanism. We carried out this test at all trial point-sources

adjacent to Position 33 (the optimum position of Event I). The results of this test are shown in

Supplementary Table 7. For all but one position of Event I, the position, timing, and mechanism

of Event II remain consistent with the optimum solution. When Event I is fixed to Position 25,

the MT solution of Event II appears less stable. However, Position 25 is directly adjacent to

Position 16 (the optimum location of Event II from ID; Fig. 2b), so this discrepancy is expected

because the inversion tries to explain both events at this position with a single source. In

summary, we find that the Event II solution is stable with respect to the exact position and

mechanism of Event I.

Mesh design for the 3-D waveform simulation

358

359 For the wave propagation simulations, we constructed a hexahedral unstructured mesh using

360 the GEOCUBIT software package[27]. The lateral resolution at the surface is 5 km, coarsening at

361 a refinement layer (45 km depth, which is an average Moho depth for the region[15,16]). The mesh

362 honours surface relief and bathymetry to ensure that topographic effects on waveform

363 propagation are accurately simulated. Our mesh does not contain dipping geological

364 discontinuities in the subsurface, such as the oceanic Moho, due to the lack of constraints on its

365 geometry. This mesh has been designed for simulations that are accurate up to ~0.3 Hz, well

366 above the maximum frequency of our waveform inversions, ensuring numerically stable

367 simulations. The Mesh used is shown in Supplementary Figure 13.